Computation of Navier-Stokes Solutions Exhibiting Asymmetric Vortices

M. J. Siclari* and F. Marconi*
Grumman Corporate Research Center, Bethpage, New York

An efficient Navier-Stokes solver is used to demonstrate the existence of asymmetric vortex flows on slender cones flying at supersonic speeds and at very high angles of attack. The iteration scheme is continued until the residual or error is reduced to machine zero. The computations were carried out on very fine grids so that issues of unsteadiness in the solution or large truncation error are minimized. These types of asymmetries have been noted experimentally for years; in addition, inviscid analytical/computational models have indicated the existence of these types of solutions. This paper is the first to present Navier-Stokes solutions which firmly demonstrate that these flows exist and that they are not experimental or computational anomalies.

Introduction

In the late 1940s, the phenomenon of lateral instability due to asymmetric vortex formation was discovered. On slender-nosed aircraft flying at a high angle of attack ($\alpha >$ twice the nose half-angle), the flow (which at lower α was symmetric about the plane containing the freestream velocity vector) could be very asymmetric due to the generation of asymmetric vortices. While the separation points may be slightly asymmetric, the resulting vortices are very asymmetric, which results in large sideforces. The sudden onset of the sideforce may result in lateral instability. The cause of this asymmetry has been debated since it was first discovered.

One of the first indications that this phenomenon was not due to asymmetric imperfections in experimental apparatus and was, in fact, inviscid in nature came from the work of Fiddes.[1] He showed small disturbance calculations with vortex sheets modeled by vortex filaments that exhibited asymmetric vortices. The geometry was a slender cone, and the flow was incompressible. Fiddes showed that two families of solutions existed for a symmetrically separated flow. One family had a single symmetric solution, and the resulting vortices were symmetric; the second family had two asymmetric solutions. The second family asymmetric solutions are simply mirror images of each other, but they are very distinct from the first family symmetric flow. The asymmetric solutions exist only in the very high angle-of-attack regime (α greater than twice the cone half-angle). At these conditions, the asymmetric solution compares much better with experimental data than the symmetric one. The question of whether the small disturbance approximation could be the cause of the asymmetry in Fiddes' computation was answered by the Euler computations of Marconi.[2] An Euler computation was used in conjunction with a flow-separation model to predict asymmetric flows in the same incidence regime as Fiddes. It should be pointed out that the study of Ref. 2 was carried out in the supersonic regime as is the present study. Unlike Fiddes, the symmetric solution was found to be unstable in the Euler computation. The only way to achieve a symmetric solution was to enforce a symmetry condition. If the symmetry conditions were relaxed after a symmetric solution was converged, the solution would revert to an asymmetric behavior. The present paper will substantiate the work of Fiddes and Marconi by presenting evidence of valid asymmetric Navier-Stokes solutions on cones at supersonic speed. The present work goes beyond Refs. 1 and 2 in that no model needs to be assumed at the separation point or vortex since the time-averaged Navier-Stokes equations are solved.

The computational procedure (see Ref. 3) used in the present study will be briefly outlined in the next section. In a subsequent section, half-plane symmetric results will be presented. Then, the symmetry condition imposed on the half-plane will be eliminated, and full plane computational results will be shown.

Computational Procedure

The conical flow equations for viscous and inviscid flow represent a subset of the general Navier-Stokes equations. The unsteady Navier-Stokes equations in conservation form and Cartesian coordinates can be written as

$$\frac{\partial \boldsymbol{Q}}{\partial t} + \frac{\partial (\boldsymbol{F} - \boldsymbol{F}_v)}{\partial x} + \frac{\partial (\boldsymbol{G} - \boldsymbol{G}_v)}{\partial y} + \frac{\partial (\boldsymbol{H} - \boldsymbol{H}_v)}{\partial z} = 0 \qquad (1)$$

where the vectors $\boldsymbol{F}$, $\boldsymbol{G}$, and $\boldsymbol{H}$ are the inviscid terms and $\boldsymbol{F}_v$, $\boldsymbol{G}_v$, and $\boldsymbol{H}_v$ represent the viscous shear stress and heat flux terms. The conservation variables and flux vectors are defined as follows:

$$\boldsymbol{Q} = \begin{bmatrix} \rho \\ \rho u \\ \rho v \\ \rho w \\ e \end{bmatrix} \quad \boldsymbol{F} = \begin{bmatrix} \rho u \\ \rho u^2 + p \\ \rho uv \\ \rho uw \\ \rho uh \end{bmatrix} \quad \boldsymbol{G} = \begin{bmatrix} \rho v \\ \rho vu \\ \rho v^2 + p \\ \rho vw \\ \rho vh \end{bmatrix} \quad \boldsymbol{H} = \begin{bmatrix} \rho w \\ \rho wu \\ \rho wv \\ \rho w^2 + p \\ \rho wh \end{bmatrix}$$

$$\boldsymbol{F}_v = \begin{bmatrix} 0 \\ \tau_{xx} \\ \tau_{xy} \\ \tau_{xz} \\ F_h \end{bmatrix} \quad \boldsymbol{G}_v = \begin{bmatrix} 0 \\ \tau_{xy} \\ \tau_{yy} \\ \tau_{yz} \\ G_h \end{bmatrix} \quad \boldsymbol{H}_v = \begin{bmatrix} 0 \\ \tau_{xz} \\ \tau_{yz} \\ \tau_{zz} \\ H_h \end{bmatrix}$$

where u, v, and w are the Cartesian velocity components in the x, y, and z directions, respectively; ρ is the density; p the pressure; and e the total energy. The pressure and total en-

Received June 29, 1989; revision received Feb. 15, 1990.

*Senior Staff Scientist. Associate Fellow AIAA.

thalpy are related to the flow variables by

$$e = \frac{p}{\gamma - 1} + \frac{1}{2}\rho(u^2 + v^2 + w^2)$$

$$h = \frac{e + p}{\rho} \tag{2}$$

where γ is the ratio of specific heats.

The Cartesian equations can be transformed to a spherical or conical coordinate system by the following transformation:

$$\bar{x} = x/z,\ \bar{y} = y/z \qquad \text{and} \qquad R^2 = x^2 + y^2 + z^2 \tag{3}$$

If all lengths are scaled by L, density and velocities by the freestream density (ρ_∞) and speed of sound (a_∞), energy and pressure by ($\rho_\infty a_\infty^2$), and time by (L/a_∞), the dimensionless Navier-Stokes equations can be rewritten in spherical or conical coordinates as

$$\frac{\partial \boldsymbol{Q}}{\partial t} + \frac{\Omega}{R}\left[\frac{\partial}{\partial \bar{x}}\left(\bar{F} - \frac{1}{R_e}\bar{F}_v\right) + \frac{\partial}{\partial \bar{y}}\left(\bar{G} - \frac{1}{R_e}\bar{G}_v\right) + 2 \times \left(\bar{I} - \frac{1}{R_e}\bar{I}_v\right)\right] + \frac{1}{\Omega}\frac{\partial}{\partial R}\left(\bar{H} - \frac{1}{R_e}\bar{H}_v\right) = 0 \tag{4}$$

where the flux vectors ($\bar{F}$, $\bar{G}$, $\bar{H}$, $\bar{I}$) and ($\bar{F}_v$, $\bar{G}_v$, $\bar{H}_v$, $\bar{I}_v$) are defined as

$$\bar{F} = \begin{bmatrix} \rho\bar{U} \\ \rho u\bar{U} + p \\ \rho v\bar{U} \\ \rho w\bar{U} - \bar{x}p \\ \rho h\bar{U} \end{bmatrix} \qquad \bar{G} = \begin{bmatrix} \rho\bar{V} \\ \rho u\bar{V} \\ \rho v\bar{V} + p \\ \rho w\bar{V} - \bar{y}p \\ \rho h\bar{V} \end{bmatrix}$$

$$\bar{H} = \begin{bmatrix} \rho\bar{W} \\ \rho u\bar{W} + \bar{x}p \\ \rho v\bar{W} + \bar{y}p \\ \rho w\bar{W} + p \\ \rho h\bar{W} \end{bmatrix} \qquad \bar{I} = \begin{bmatrix} \rho w \\ \rho uw \\ \rho vw \\ \rho w^2 + p \\ \rho hw \end{bmatrix}$$

$$\bar{F}_v = \begin{bmatrix} 0 \\ \tau_{xx} - \bar{x}\tau_{xz} \\ \tau_{xy} - \bar{x}\tau_{yz} \\ \tau_{xz} - \bar{x}\tau_{zz} \\ F_h - \bar{x}H_h \end{bmatrix} \qquad \bar{G}_v = \begin{bmatrix} 0 \\ \tau_{xy} - \bar{y}\tau_{xz} \\ \tau_{yy} - \bar{y}\tau_{yz} \\ \tau_{yz} - \bar{y}\tau_{zz} \\ G_h - \bar{y}H_h \end{bmatrix}$$

$$\bar{H}_v = \begin{bmatrix} 0 \\ \bar{x}\tau_{xx} + \bar{y}\tau_{xy} + \tau_{xz} \\ \bar{x}\tau_{xy} + \bar{y}\tau_{yy} + \tau_{yz} \\ \bar{x}\tau_{xz} + \bar{y}\tau_{yz} + \tau_{zz} \\ \bar{x}F_h + \bar{y}G_h + H_h \end{bmatrix} \qquad \bar{I}_v = \begin{bmatrix} 0 \\ \tau_{xz} \\ \tau_{yz} \\ \tau_{zz} \\ H_h \end{bmatrix}$$

and

$$\bar{U} = u - \bar{x}w$$

$$\bar{V} = v - \bar{y}w$$

$$\bar{W} = u\bar{x} + v\bar{y} + w$$

$$\Omega = (1 + \bar{x}^2 + \bar{y}^2)^{1/2}$$

$$(R_e)^{-1} = M_\infty / R_{e\infty}$$

Assuming Stokes' hypothesis, the shear stress and heat flux terms become

$$\tau_{xx} = 2\bar{\mu}u_x - \sigma \qquad \tau_{xy} = \bar{\mu}(u_y + v_x)$$
$$\tau_{yy} = 2\bar{\mu}u_y - \sigma \qquad \tau_{xz} = \bar{\mu}(u_z + w_x)$$
$$\tau_{zz} = 2\bar{\mu}u_z - \sigma \qquad \tau_{yz} = \bar{\mu}(v_z + w_y)$$

$$F_h = u\tau_{xx} + v\tau_{xy} + w\tau_{xz} + A\bar{\mu}\,a_x^2$$
$$G_h = u\tau_{xy} + v\tau_{yy} + w\tau_{yz} + A\bar{\mu}\,a_y^2$$
$$H_h = u\tau_{xz} + v\tau_{yz} + w\tau_{zz} + A\bar{\mu}\,a_z^2$$

where

$$\sigma = \tfrac{2}{3}\,\bar{\mu}(u_x + v_y + w_z), \qquad A = [P_r(\gamma - 1)]^{-1}$$

and Sutherland's law has been assumed for the viscosity:

$$\bar{\mu} = a^3\left[\frac{1 + S}{a^2 + S}\right]$$

and S is a constant.

It has been shown in the work of Fiddes[1] and Marconi[2] that the assumption of conical flow has no effect on the essential features of asymmetric vortex flows. The quasi-two-dimensional nature of conical flow eliminates some numerical issues in that very fine grids can be used, and the iteration can be carried out to machine zero in a small amount of computer time. The assumption of laminar flow does not affect these phenomena either, again indicated in Refs. 1 and 2.

Assuming that the R derivatives vanish in conical flow, the crossflow terms in Eq. (4) can be written in integral form as

$$\frac{\partial}{\partial \hat{t}}\iint_S \boldsymbol{Q}\,d\bar{x}\,d\bar{y} + \oint(\hat{F}\,d\bar{y} - \hat{G}\,d\bar{x}) + 2\iint \hat{I}\,d\bar{x}\,d\bar{y} \tag{5}$$

where

$$\hat{F} = \bar{F} - \frac{1}{Re}\bar{F}_v$$

$$\hat{G} = \bar{G} - \frac{1}{Re}\bar{G}_v$$

$$\hat{I} = \bar{I} - \frac{1}{Re}\bar{G}_v$$

$$\hat{t} = \frac{\Omega}{R}t$$

The coordinate coefficient metric Ω/R has been absorbed into the unsteady term since only steady-state solutions are sought.

A node-centered finite volume scheme is applied to a discretized version of Eq. (5) in the crossflow plane. Figure 1 illustrates the basic scheme. Both the flow variables Q and the residuals are stored at node points. The cell-centered fluxes are first computed over each cell of the grid by summing the fluxes across the four individual sides of the cell in a fashion similar

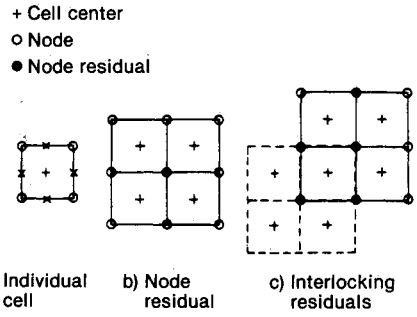

Fig. 1 Schematic of node-centered finite volume scheme.

to a cell-centered scheme. Unlike the cell-centered scheme, the flow variables are stored at the endpoints of each side constituting the boundaries of a cell. This has the potential of yielding a more accurate estimate for the flux across the sides of a highly skewed or irregular mesh than that provided by a cell-centered scheme. The residual at each node point is then computed by summing the cell-centered fluxes of the four cells surrounding that node point. In discretized form, the conical terms of Eq. (5) can be written at a node point i,j as

$$\Delta S\frac{\Delta Q}{\Delta \hat{t}}+\sum_{\text{cell}=1}^{4}\sum_{\text{side}=1}^{4}(\hat{F}\Delta\bar{y}-\hat{G}\Delta\bar{x})+2\hat{I}\Delta S=0 \tag{6}$$

where $\hat{F}$ and $\hat{G}$ are the total side fluxes that include viscous terms at the node points. The area ΔS is defined as

$$\Delta S=\sum_{\text{cell}=1}^{4}\Delta A$$

and is the sum of the areas of the four individual cells surrounding a node point. Thus, the node residuals correspond to flux balances on interlaced control volumes, each consisting of a group of four cells.

To include the viscous shear stress and heat flux terms, the velocity derivatives are estimated at the node points using central difference formulas in a computational space. The mesh transformation derivatives needed for the velocity derivatives are computed numerically. At the boundary, one-sided differences are used to estimate the velocity derivatives.

A blend of second- and fourth-order differences is used for added artificial dissipation. The fourth-order differences are added as background dissipation to prevent odd and even point decoupling. The second-order differences are added primarily to smooth out oscillations in regions of severe pressure gradients associated with shock waves. A detailed account of the form of the dissipation can be found in Refs. 3–5. As a numerical experiment, both these dissipations were eliminated in the boundary layer where physical dissipation is high enough to stabilize the solution. This test indicated that the artificial dissipation was small enough so as not to overwhelm the real dissipation.

The set of unsteady governing equations can be represented as

$$\frac{\partial Q}{\partial t}+\frac{1}{\Delta S}R_{\bar{x}\bar{y}}(Q)+\frac{1}{\Delta S}D_{\bar{x}\bar{y}}(Q)=0 \tag{7}$$

where the operator $R_{\bar{x}\bar{y}}$ represents the crossflow finite volume spatial approximation to the residual, and $D_{\bar{x}\bar{y}}$ represents the added artificial dissipation. A modified fourth-order Runge-Kutta scheme is used to integrate the set of ordinary differential equations defined by Eqs. (6) and (7) in the following manner:

$$Q^{(l)}=Q^{(0)}-\alpha_l\frac{\Delta t}{\Delta S}(R_{\bar{x}\bar{y}}{}^{(l-1)}+D_{\bar{x}\bar{y}}{}^{(0)} \tag{8}$$

where

$$\alpha_l=\left(\frac{1}{4},\frac{1}{3},\frac{1}{2},1\right)$$

The bracketed superscript in Eq. (8) refers to the stages of the Runge-Kutta scheme. The dissipative terms are frozen throughout the multistage integration scheme. The local time step is taken to be

$$\Delta t=CFL\ \Delta t^*$$

In addition, implicit residual smoothing is utilized in the crossflow plane to accelerate convergence. The residual smoothing is applied to alternate stages, the second and the fourth stage, of the Runge-Kutta scheme.

A multigrid method is used to accelerate the convergence of the basic multistage time stepping scheme. The idea behind the multigrid scheme is to speed up the evolution process by using a series of coarser grids that introduce larger scales and larger time steps while requiring less costly computations. The present multigrid scheme follows the work of Jameson[5] and is presented in more detail in Ref. 3.

The method begins by first computing one or more time steps on a fine grid denoted as the first grid $m = 1$. Successively coarser grids are then generated by eliminating alternate points in each coordinate direction.

On the coarse grids $m > 1$, the multistage time stepping scheme is modified by a forcing function, so that the solution on the successively coarser grids $m + 1$, is driven by the residuals computed on the finer grids m. Thus, in the first stage, the forcing function simply cancels the coarse grid residual and replaces it by a weighted sum of the fine grid residuals.

After one or more time steps are carried out on a given grid, the process is repeated until the coarsest grid is reached. The accumulated corrections are now transferred upward from each grid to the next finer grid by an interpolation process. The correction transferred up from a given grid includes both the correction calculated on that grid and the sum of the corrections interpolated from coarser grids in the sequence.

Discussion of Results

Laminar Navier-Stokes solutions, with the assumption of conical flow (i.e., $\partial/\partial R = 0$) are computed for a 5-deg circular cone ($\theta = 5$ deg) at $M_\infty = 1.80$ for a variety of high angles of attack (i.e., $\alpha/\theta \geq 2$). All the solutions are computed to machine zero (i.e., until the computer roundoff error has been reached). The solutions were computed on a CRAY XMP with 64-bit accuracy. Machine zero occurs around 10^{-11} to 10^{-12} or after a 14–15 order of magnitude drop in the residual. The reason or necessity for this accuracy will become obvious in a later section.

Figure 2 shows typical crossflow plane entropy contours for solutions generated on a half-plane grid of (81 × 81) points

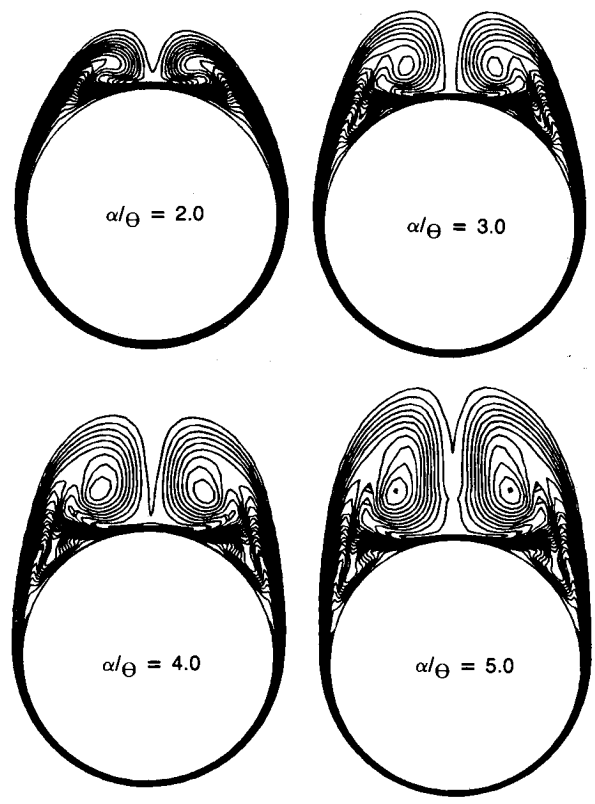

Fig. 2 Entropy contours for 5-deg cone at $M_\infty = 1.80$, $Re = 1 \times 10^5$ at various incidences computed on a half-plane grid with symmetry enforced.

at $M_\infty = 1.80$ and $\alpha/\theta = 2$, 3, 4, and 5, and a Reynolds number of 1×10^5. The entropy contours depict the boundary layer that separates on the leeward plane generating a primary vortex and secondary vortices due to the separation of the reverse crossflow. These symmetric solutions were computed by enforcing symmetry in the windward and leeward planes and are presented to demonstrate the standard half-plane viscous solutions.

Full Plane Solutions

The code was modified to compute solutions on a full plane grid. Figure 3 shows an example of this grid, which is an identical reflection of the half-plane grid. The grid outer boundary is adjusted to capture the bow shock generated by the cone and to resemble its shape for higher accuracy. The grid is divided evenly around the cone, and it is stretched in the direction normal to the body to resolve the inviscid features of the vortex in the leeward plane. To resolve the boundary layer, a sublayer grid is embedded in the basic inviscid grid near the surface as shown in Fig. 3b. Without disturbing the inviscid grid, an inviscid grid line around the cone (near its surface) is selected, and 16–24 points are patched into the sublayer grid using a geometric function typically used for turbulent boundary layers. The grids were designed to have a minimum of 10–15 points in the windward boundary layer. For full plane solutions, a 161×81 grid was used. The grid cut was located in the windward plane so as not to introduce any uncertainty with respect to numerical issues that might arise in the leeward plane.

Figure 4 shows a typical set of results computed on a full plane grid at $\alpha = 10$ deg or $\alpha/\theta = 2$. Figure 4a shows the isobars and Fig. 4b shows the crossflow velocity vectors near the leeward surface. The computed solution at $\alpha/\theta = 2$ is completely symmetric demonstrating that the computational procedure used can produce perfectly symmetrical solutions on a full plane grid when they exist.

Figure 5 shows the corresponding full plane convergence history plot of the logarithm to the base 10 of the maximum residual vs multigrid cycle for $\alpha/\theta = 2$ and $M_\infty = 1.8$ with a Reynolds number of 1×10^5. The solution converges to machine zero at around 1300 multigrid cycles. For practical purposes, the solution has been achieved in about 200–300 multigrid cycles. The solution was allowed to continue beyond

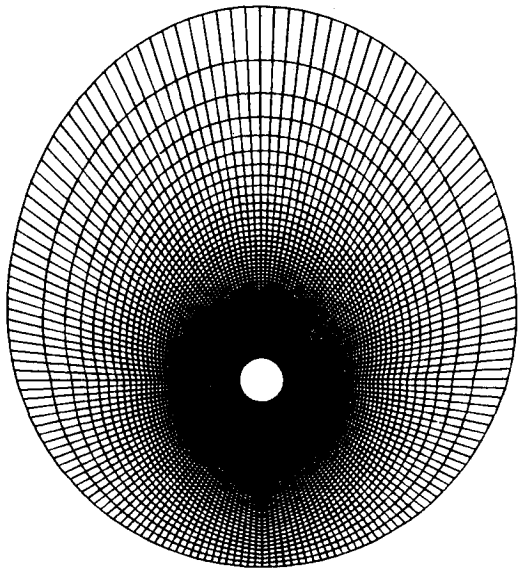

a) Grid

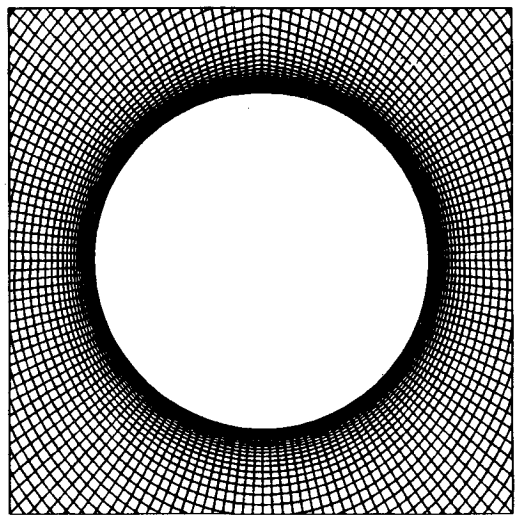

b) Grid near surface

Fig. 3 Full plane computational grid used for 5-deg cone at $M_\infty = 1.80$, $\alpha/\theta = 2$, $Re = 1 \times 10^5$.

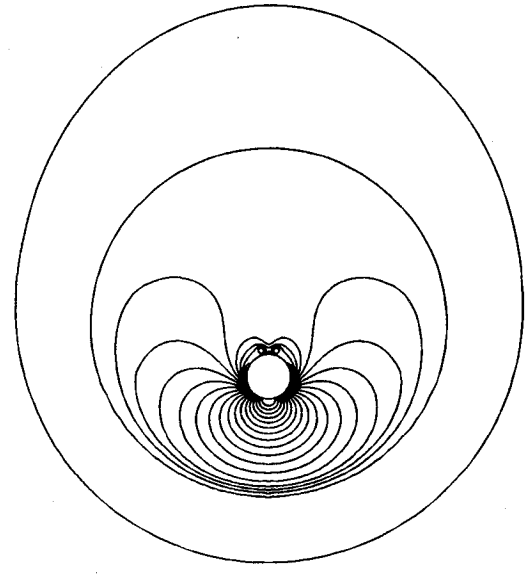

a) Isobars

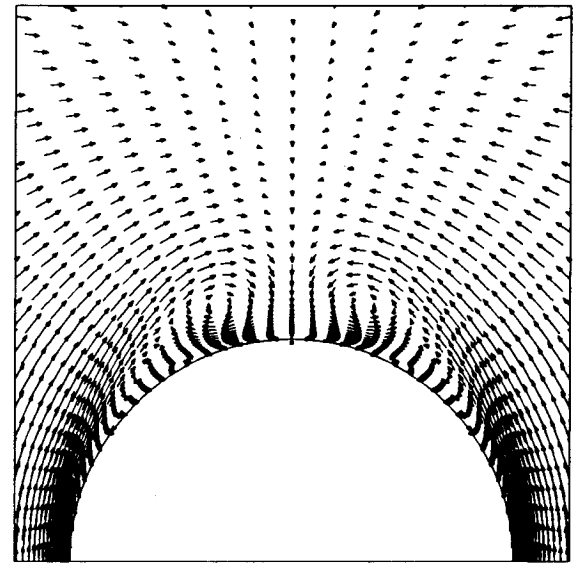

b) Velocity vectors near lee surface

Fig. 4 Symmetric flowfield computed for 5-deg cone at $M_\infty = 1.80$, $\alpha/\theta = 2$, $Re = 1 \times 10^5$.

machine zero for more than 1000 multigrid cycles where the truncation error causes the maximum residual to bounce around machine zero. This shows that the numerical scheme is stable and remains at machine zero for this stable symmetric solution.

Convergence Study of Asymmetric Solutions

Figure 6 shows a full plane convergence history plot at a higher angle of attack of 20 deg ($\alpha/\theta = 4$) for the same circular cone and Reynolds number. The computation is started from symmetric freestream conditions. In the first attempt at seeking asymmetric solutions, these flow conditions were run, and the numerical scheme was halted when the residual reached 10^{-5} (i.e., the error declined by about nine orders of magnitude). It was thought that, if the asymmetry had not appeared by this point, it did not exist. Past experience indicated that, beyond a five or six order of magnitude decline in maximum residual, no significant changes took place in the solution. As Fig. 6 illustrates, the residual declines in magnitude by about 10 orders and then begins to increase for about 1000 multigrid cycles to almost its original level and then begins to decline again. At approximately 3500 multigrid cycles, the scheme reaches machine zero and stays at machine zero for more than 1000 multigrid cycles. The flowfield at the first minimum in the residual (at about 500 multigrid cycles) and that at machine zero were both studied. The two "solutions" are indicated by the crossflow streamline patterns inset on the figure. The first minimum reached corresponds to a

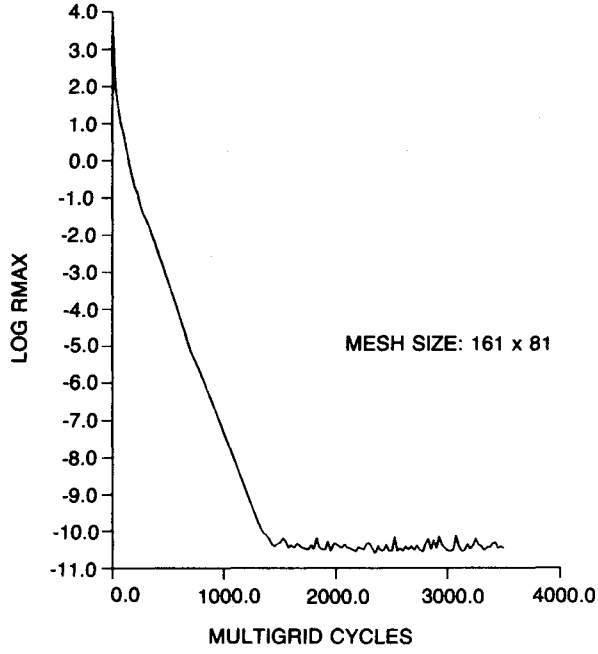

Fig. 5 Convergence history of the maximum residual for the 5-deg cone at $M_\infty = 1.80$, $\alpha/\theta = 2$, $Re = 1 \times 10^5$ starting with symmetric initial freestream conditions.

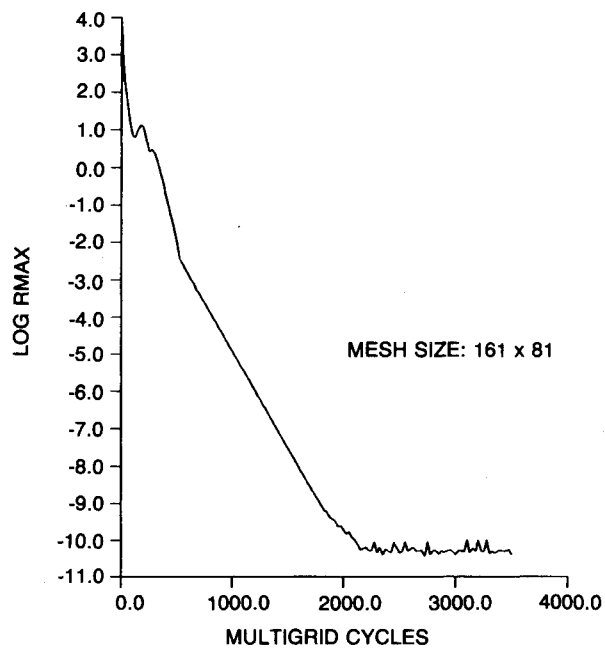

Fig. 7 Convergence history of the maximum residual for the 5-deg cone at $M_\infty = 1.80$, $\alpha/\theta = 4$, $Re = 1 \times 10^5$ starting with asymmetric initial freestream conditions (i.e., 2 deg of sideslip).

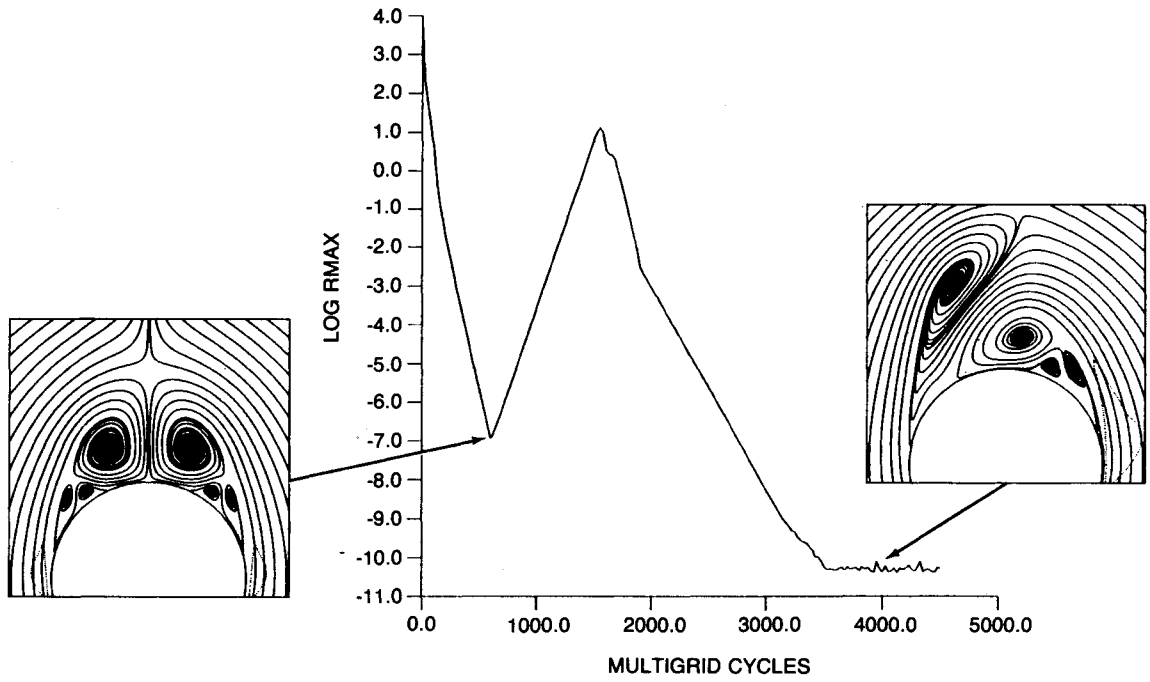

Fig. 6 Convergence history of the maximum residual for the 5-deg cone at $M_\infty = 1.80$, $\alpha/\theta = 4$, $Re = 1 \times 10^5$ starting with symmetric initial freestream conditions.

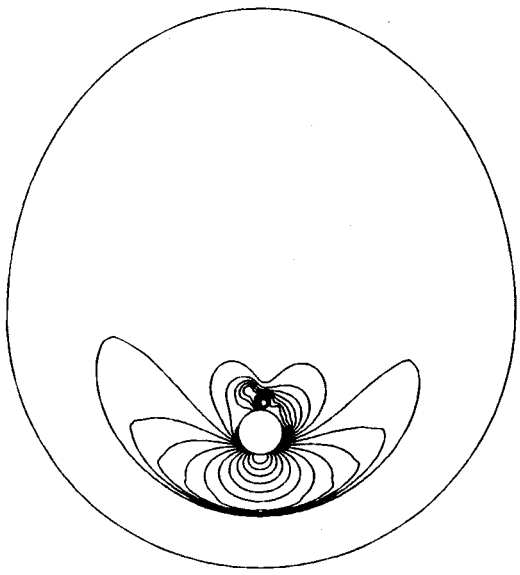

a) Isobars

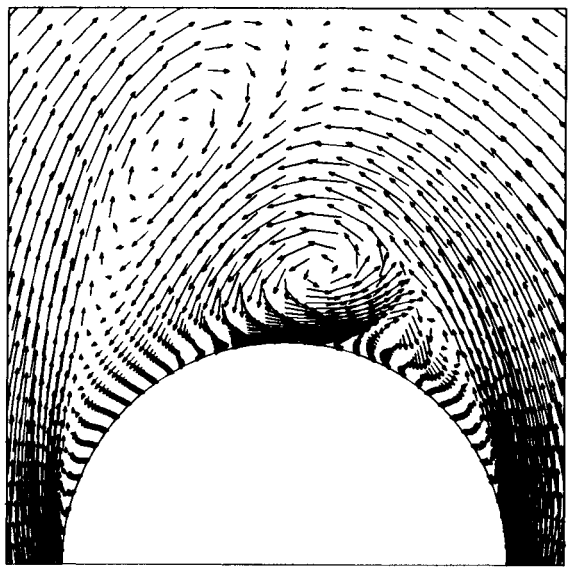

b) Velocity vectors near lee surface

Fig. 8 Asymmetric flowfield computed for the 5-deg cone at M_∞ = 1.80, α/θ = 4, Re = 1 × 10^5.

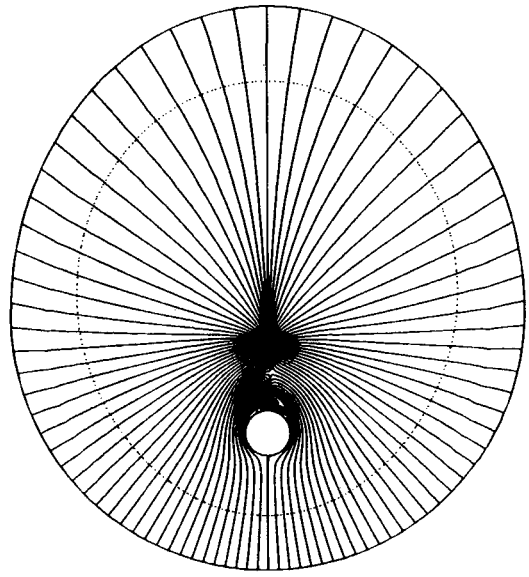

a) Streamline pattern

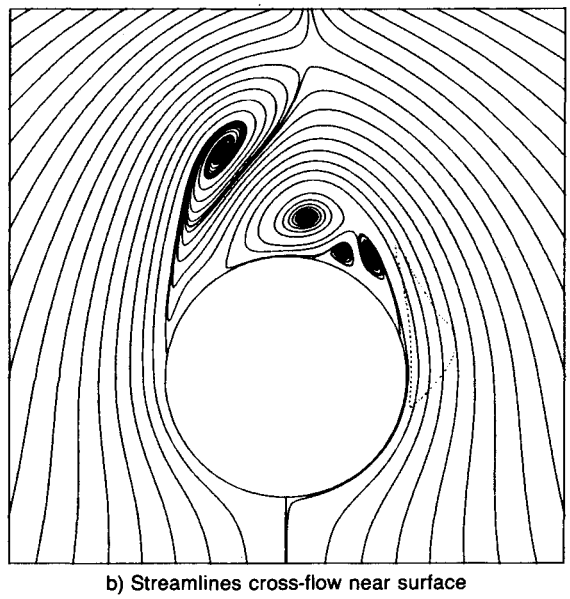

b) Streamlines cross-flow near surface

Fig. 9 Asymmetric crossflow streamline pattern computed for 5-deg cone at M_∞ = 1.80, α/θ = 4, Re = 1 × 10^5.

symmetric result, and the final machine zero result corresponds to the asymmetric solution. It must be concluded that the symmetric result is unstable since machine zero cannot be maintained for this solution. This was verified by running other angles of attack (all above the critical α) with symmetric initial conditions, and the symmetric result always proved to be unstable. In fact, in some of the cases that were studied, the symmetric result would actually attain machine zero, but it could not remain at machine zero and would pop up and, finally, converge to the asymmetric solution and remain there.

Figure 7 shows another convergence plot for the same condition (α/θ = 4). In this case, the computation was started from slightly asymmetric initial conditions. The initial conditions were such that there was a small angle of sideslip (2 deg) introduced into the internal flow. It should be mentioned that the outer boundary conditions always correspond to fixed symmetric freestream conditions. This is implemented and held fixed during the iteration scheme at two grid rings defining the outer grid boundary. For these asymmetric initial conditions, as indicated by Fig. 7, the convergence is monotonic to machine zero. The resulting solution is the asymmetric solution identical to that obtained with the symmetric initial conditions. To remove any doubts about the stability of the asymmetric solution, machine zero was maintained for 1500 multigrid cycles.

Hence, a monotonic convergence to the asymmetric solution could be achieved if a small asymmetry were introduced into the initial conditions. The fact that the asymmetric solution could be achieved in two different ways reinforces the validity of these solutions. If the asymmetric solutions could be achieved only from an asymmetric perturbation to the initial conditions, one might think that the asymmetric solution could possibly be a result of some trapped vorticity or dissipation in the numerical evolution of such a solution. Figure 8 shows the isobars and crossflow velocity vectors for α = 20 deg (α/θ = 4). The pressure contours show that the asymmetry is primarily a local effect in the vicinity of the leeward vortices. The asymmetry of the computed solution is more clearly shown in the velocity vector plot. The velocity vector plot shows that secondary separation exists on the right side of the cone; whereas the reverse flow is attached on the left side. The crossflow streamlines for the entire crossflow

plane are shown in Fig. 9a. This figure indicates that the local asymmetry diminishes quickly as the outer boundary is approached. Again, it should be pointed out that symmetric conditions are imposed on the outer boundary. Figure 9b shows the crossflow streamline pattern in the vincinity of the vortex interaction zone, and the asymmetry of the solution is indicated quite clearly.

Detailed Study of Asymmetric Solutions

A study of the extent of the occurrence of asymmetric viscous laminar solutions was carried out for the 5-deg cone at $M_\infty = 1.80$ and Reynolds number of 1×10^5. All of the computations were carried out on a fine grid of 161 × 81. This study would not have been possible except for the fact that the current code is very efficient. All of the solutions were converged to machine zero and continued for some time in order to test their stability. To achieve monotonic convergence (see Fig. 7), all of the solutions were carried out using slightly asymmetric initial freestream conditions corresponding to ±2 deg of sideslip. This technique reduces the multigrid cycles required for convergence by almost a factor of two. Thus far, only one of the asymmetric solutions has been mentioned, and it should be made clear that there are two; one is the mirror image of the other.

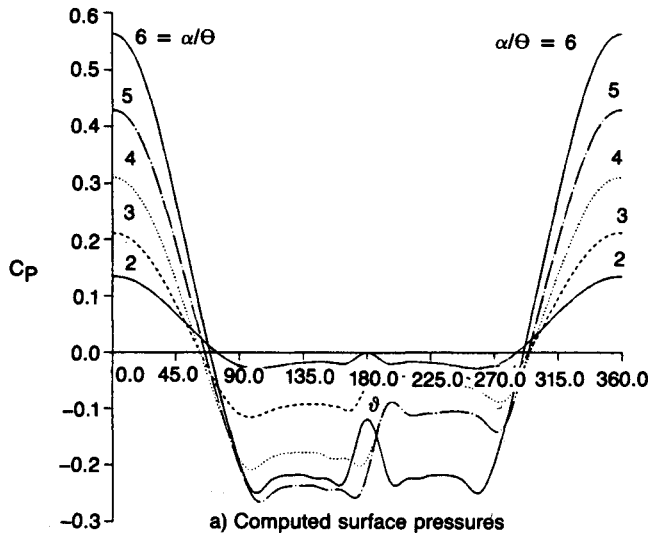

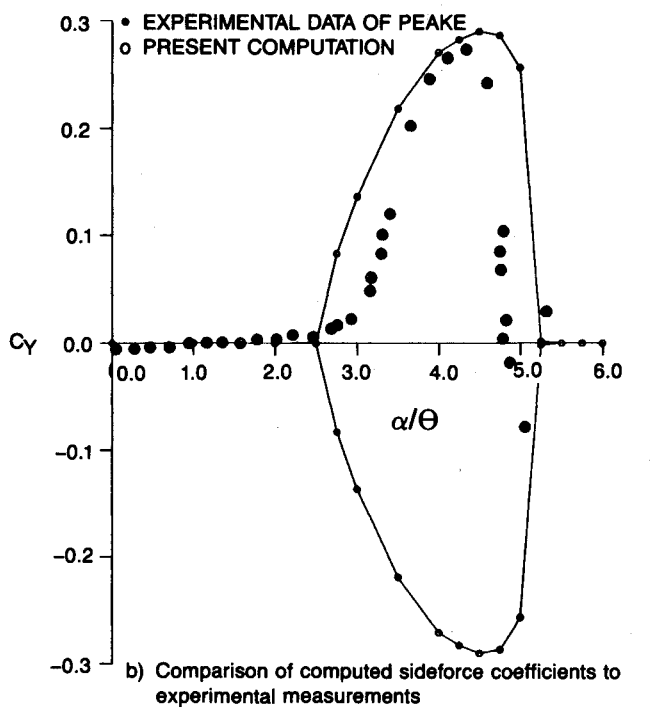

Fig. 10 Computed sideforce coefficients and surface pressures for the 5-deg cone at $M_\infty = 1.80$, $\alpha/\theta = 4$, $Re = 1 \times 10^5$.

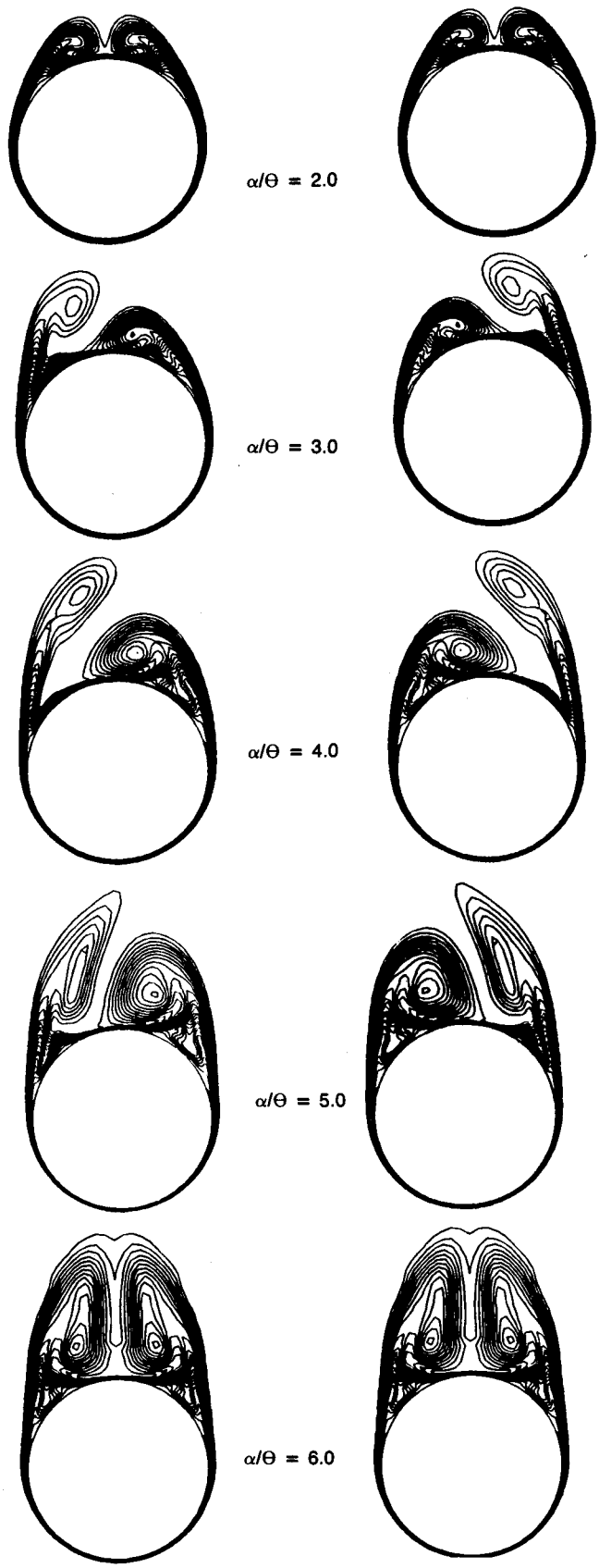

Fig. 11 Computed entropy contours for 5-deg cone at $M_\infty = 1.80$ for incidences ranging from $\alpha/\theta = 2$ to 6 showing the bifurcation of the solutions.

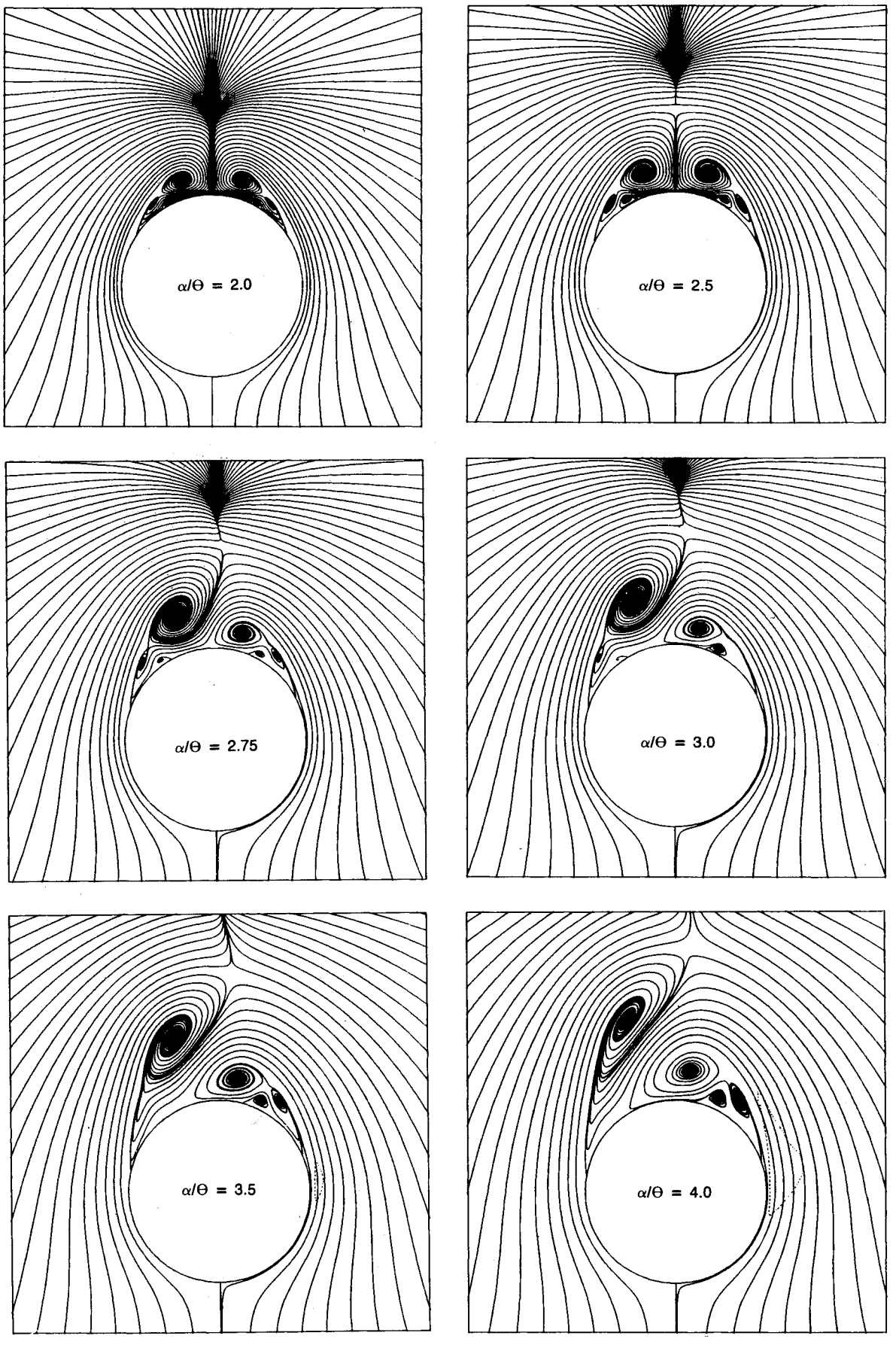

Fig. 12 Computed crossflow streamline patterns for 5-deg cone at $M_\infty = 1.80$, $Re = 1 \times 10^5$ for incidences ranging from $\alpha/\theta = 2$ to 4, prior to maximum asymmetry.

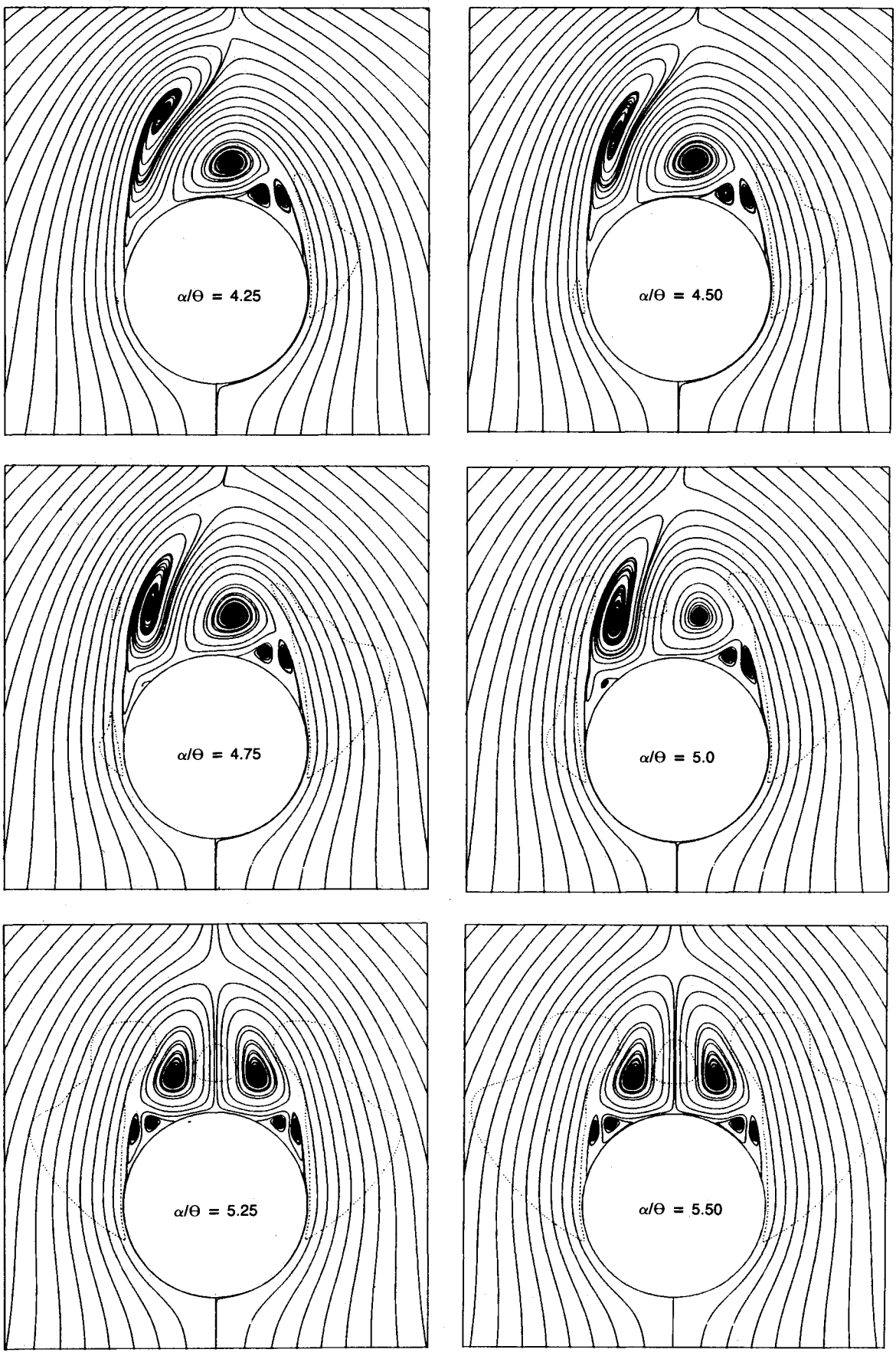

Fig. 13 Computed crossflow streamline patterns for 5-deg cone at M_∞, $Re = 1 \times 10^5$ for incidences ranging from $\alpha/\theta = 4.25$ to 5.50.

Local vortex asymmetry has a significant effect on the surface pressure distribution. Figure 10a shows several examples of computed surface pressures for both symmetric solutions and one root of the asymmetric solutions. Steady asymmetric flows were observed experimentally by Peake[6] and the sideforces on a 5-deg cone were measured for a range of Mach numbers. Figure 10b shows the experimental sideforce coefficient data plotted as a function of relative incidence α/θ for $M_\infty = 1.8$. Also plotted are the results of the present study. Remarkably good agreement is indicated for the peak value of sideforce and domain of occurrence of these asymmetric flows. It should be noted that the experimental data are at a higher Reynolds number and the flow is probably turbulent; while the present solutions are conical and all laminar. The numerical results indicate the onset of asymmetric flow at $\alpha/\theta = 2.5$ with a peak in terms of sideforce at about $\alpha/\theta = 4.5$. The experimental data exhibit a similar, but slightly narrower, range for the asymmetric behavior. One of the more notable and surprising results of the numerical study is that the asymmetry disappears rather abruptly at even higher incidences, and the solutions return to symmetry. This was observed in the experimental data; the sideforce dropped rapidly at $\alpha/\theta = 4.8$. In the experiment, the flow was unsteady for $\alpha/\theta > 5$.

It should be pointed out that in Fig. 10b the sideforce corresponding to both asymmetric solutions are shown, positive and negative force. The symmetric solution bifurcates at around $\alpha/\theta = 2.50$ and returns to symmetry at about $\alpha/\theta = 5$. Which solution shows up numerically depends upon the initial condition. For the most part, when the iteration is started with positive sideslip initial conditions, one type of solution will result. This occurred in the majority of cases run, but there were exceptions to this rule probably due to the small values of sideslip used. Figure 11 illustrates the bifurcation of the numerical solutions in terms of the computed entropy contours starting at $\alpha/\theta = 2$ and returning to symmetry by 6.

One of the more interesting features of the asymmetric solutions discovered here is the complex vortex patterns that evolve. These are vividly illustrated in the crossflow streamline patterns of Fig. 12. All of the streamline patterns shown in Fig. 12 correspond to one root of the bifurcation. Figure 12 shows the evolution of the asymmetric behavior from the $\alpha/\theta = 2$ symmetric solution to an incidence just prior to the peak sideforce at $\alpha/\theta = 4$. At $\alpha/\theta = 2$, the solution is symmetric but separated. Three vortices occur on each side of the leeward plane with a total of six vortices appearing in this symmetric solution. The symmetric solution extends to $\alpha/\theta = 2.5$ with qualitatively similar features and with the vortices just becoming larger relative to the cone. At $\alpha/\theta = 2.75$, the asymmetric solution appears quite abruptly indicating the sensitivity to incidence. The $\alpha/\theta = 2.75$ is just a 1.25 deg increase in incidence over $\alpha/\theta = 2.5$, and the difference in the solution is quite significant (see Fig. 12). The asymmetric solution still indicates a total of six vortices. A larger primary vortex appears on the left-hand side (LHS) of the flow. The tertiary vortices diminish in size. A further increase in incidence of 1.25 deg to $\alpha/\theta = 3$ indicates the further diminishing of the LHS tertiary vortex. The secondary vortex does not appear on the right-hand side (RHS), but it is not clear whether this vortex was just missed by the streamline plotting code. A further increase in incidence to $\alpha/\theta = 3.5$ results in the disappearance of the LHS secondary and tertiary vortices resulting in one large primary vortex on the LHS and three vortices on the RHS. It should be mentioned that supersonic crossflow conditions are absent until $\alpha/\theta = 3.5$. The crossflow sonic line is indicated by the dashed curve on the RHS of the figure (for $\alpha/\theta = 3.5$). Internal to this region, the crossflow Mach number is supersonic. In the final streamline pattern at $\alpha/\theta = 4$, the supersonic crossflow region grows dramatically in size, but the pattern remains with one large primary vortex on the LHS and three smaller vortices on the RHS. The center of the primary vortex on the RHS has now situated itself close to the leeward symmetry plane.

Figure 13 illustrates the behavior in terms of the crossflow streamline patterns of the asymmetric solutions at even higher incidences as the solutions begin to return to symmetry. At $\alpha/\theta = 4.25$, a similar pattern of four vortices is shown with the three smaller vortices on one side and the larger single vortex on the opposite side. The appearance of a small second supersonic crossflow region appears on the LHS. At $\alpha/\theta = 4.5$, both supersonic crossflow regions grow in size. A further increase in incidence to 4.75 causes a second supersonic crossflow region to occur on the LHS. A small vortex has now developed under the larger primary vortex on the LHS. At $\alpha/\theta = 5$, a fourth supersonic crossflow region appears between the two primary vortices. A pattern of five vortices has now evolved. Finally, at $\alpha/\theta = 5.25$, the two supersonic crossflow regions on the LHS have now merged into a single larger region forming two large regions of supersonic crossflow on either side of the cone with a smaller supersonic crossflow region occurring between the two primary vortices. The merg-

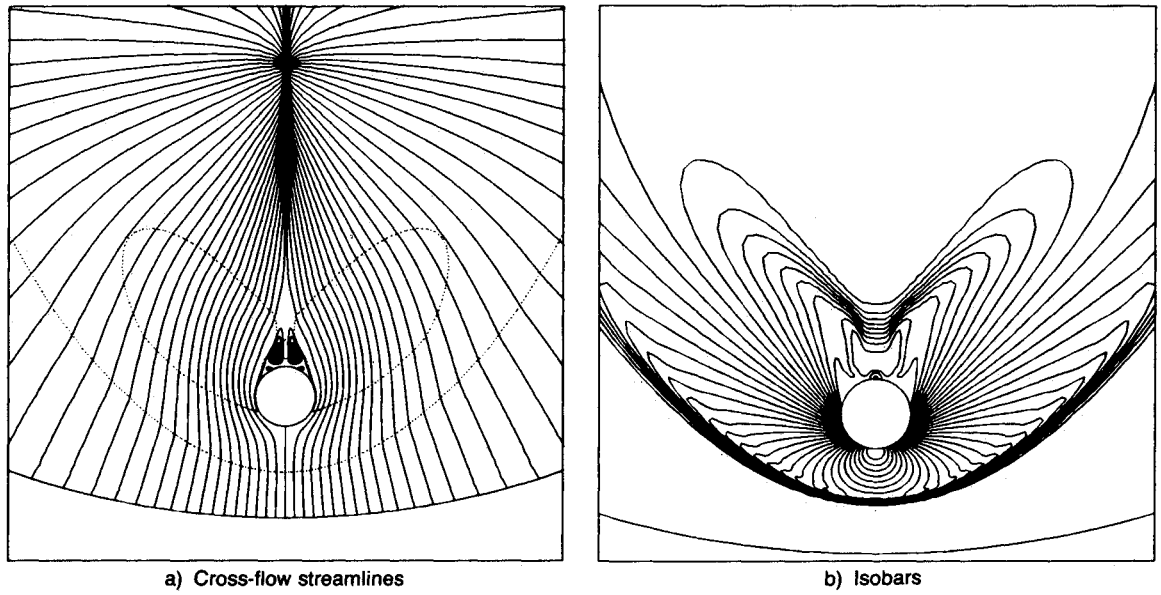

Fig. 14 Computed streamlines and isobar contours for the 5-deg cone at $M_\infty = 1.80$, $Re = 1 \times 10^5$ at very high incidence $\alpha/\theta = 9$.

ing and formation of the two opposing regions of supersonic crossflow signal the return to symmetric flow behavior and the original pattern of six symmetric vortices that existed at the lower incidences. A further increase in incidence to $\alpha/\theta = 5.5$ retains the symmetric flow behavior.

Extremely high incidences were also computed producing the crossflow streamline pattern and isobars shown in Fig. 14. In this case, $\alpha/\theta = 9$, a steady symmetric solution was computed. It should be pointed out that the experimental data of Peake indicate that the flow is unsteady for $\alpha/\theta > 5$. Figure 14 shows large supersonic crossflow regions extending from the shoulder of the cone to the leeward plane. The isobars (Fig. 14b) show the shock pattern clearly. The bow shock in the windward plane is shown to be captured quite sharply. There are large crossflow shocks near the leeward plane; the sonic lines of Fig. 14a go through the center of these shocks. These shocks sit atop the primary vortices.

Summary

Navier-Stokes solutions have been generated that indicate the existence of asymmetric, separated flow solutions at high angles of attack. The flow is assumed conical so that numerical inaccuracies can be minimized. This is the first careful study of this phenomenon with a Navier-Stokes solver, and it substantiates the analytical/computational results of Refs. 1 and 2. More importantly, the Navier-Stokes solutions compare remarkably well with the experimental findings of Ref. 6, indicating that the asymmetric solutions are well founded in the physics of the flow.

References

[1]Fiddes, S. P., "Separated Flow About Cones at Incidence-Theory and Experiment," *Studies of Vortex Dominated Flows,* edited by M. Y. Hussaini and M. D. Salas, Springer-Verlag, New York, 1985, pp. 285–310.

[2]Marconi, F., "Asymmetric Separated Flows about Sharp Cones in a Supersonic Stream," *11th International Conference on Numerical Methods in Fluid Dynamics,* edited by D. L. Dwoyer, M. Y. Hussaini, and R. G. Voigt, Springer-Verlag, Berlin, Germany, 1988, pp. 395–402.

[3]Siclari, M. J., DelGuidice, P., and Jameson, A., "A Multigrid Finite Volume Method for Solving the Euler and Navier-Stokes Equations for High Speed Flows," AIAA Paper 89-0283, Jan. 1989.

[4]Siclari, M. J., and DelGuidice, P., "A Hybrid Finite Volume Approach to Euler Solutions for Supersonic Flows," AIAA Paper 88-0225, Jan. 1988.

[5]Jameson, A., "A Vertex Based Multigrid Algorithm for Three-dimensional Compressible Flow Calculations," American Society of Mechanical Engineers Symposium on Numerical Methods for Compressible Flow, Anaheim, CA, Dec. 1986.

[6]Peake, D. J., and Own, F. K., "Control of Forebody Three-Dimensional Flow Separation," AGARD-CP-262, 1979, pp. 15-1–15-46.